CHIN. PHYS. LETT. Vol. 28, No. 3 (2011) 039601

Numerical Validation and Comparison of Three Solar Wind Heating Methods by the SIP-CESE MHD Model *

YANG Li-Ping(杨利平)[1,2**], FENG Xue-Shang(冯学尚)[1], XIANG Chang-Qing(向长青)[1],
JIANG Chao-Wei(江朝伟)[1,2]

[1]*SIGMA Weather Group, State Key Laboratory for Space Weather, Center for Space Science and Applied Research, Chinese Academy of Sciences, Beijing 100190*

[2] *College of Earth Sciences, Graduate University of Chinese Academy of Sciences, Beijing 100049*

(Received 7 December 2010)

We conduct simulations using the three-dimensional (3D) solar-interplanetary conservation element/solution element (SIP-CESE) magnetohydrodynamic (MHD) model and magnetogram data from a Carrington rotation (CR) 1897 to compare the three commonly used heating methods, i.e. the Wentzel–Kramers–Brillouin (WKB) Alfvén wave heating method, the turbulence heating method and the volumetric heating method. Our results show that all three heating models can basically reproduce the bimodal structure of the solar wind observed near the solar minimum. The results also demonstrate that the major acceleration interval terminates about $4R_S$ for the turbulence heating method and $10R_S$ for both the WKB Alfvén wave heating method and the volumetric heating method. The turbulence heating and the volumetric heating methods can capture the observed changing trends by the WIND satellite, while the WKB Alfvén wave heating method does not.

PACS: 96.50.Bh, 96.50.Ci, 96.50.Tf DOI: 10.1088/0256-307X/28/3/039601

The problem of the coronal heating and solar wind acceleration has been one of the most difficult subjects in solar and solar wind physics. There is no final solution to the problem in theoretical studies.[1,2] However, many numerical methods have been developed in the solar wind simulations to deal with it and to produce overall good results that are comparable with observations.[2−9] The most commonly used heating methods are the WKB Alfvén wave heating method (AHM), the turbulence heating method (THM) and the volumetric heating method (VHM).

In this Letter, we carry out numerical tests and comparisons to investigate the advantages and disadvantages of the three commonly used heating methods. The numerical model used here is the 3D SIP-CESE MHD model with the initial magnetic field derived from solar magnetogram data of CR 1897. The basic governing equations and details of the SIP-CESE MHD model have been described by Feng *et al.*[13,5] Here we only give some modifications.

In the AHM, the dissipation rate Q_e is added as a source term in the energy equation and Alfvén wave pressure $\varepsilon/2$ is inserted in the momentum equation. According to Refs. [7,8,10] Q_e and the control equation of ε are given by

$$\frac{\partial \varepsilon}{\partial t} + \nabla\cdot[(\boldsymbol{u}+\boldsymbol{V}_A)\varepsilon] = -0.5\varepsilon\nabla\cdot\boldsymbol{u} - Q_e,$$

$$Q_e = \frac{\rho\langle\delta u^2\rangle^{3/2}}{L_c},$$

where δu^2 is the velocity variance associated with the wave field, L_c is the correlation length of the fluctuation scale transverse to the magnetic field given by $L_c = L_{c,s}(B_s/B)^{1/2}$ (B_s is the magnetic field strength at the coronal base, $L_{c,s}$=6000 km) and $\boldsymbol{V}_A$ is the outward propagating Alfvén velocity. We set δu_s at the coronal base to be $\delta u_{s0}\sqrt{C_a}$, where $C_a = C_a'/\max(\mathrm{C_a'})$ with $C_a' = \{5.8 - 1.6e^{[1-(\theta_b/8.5)^3]}\}^{3.5}/(1+f_S)^{2/7}$ related to the expansion factor f_S and the minimum angular separation θ_b.[5] The maximum variance amplitude δu_{s0} is taken to be 35 km·s^{-1}. Evidently, δu_s increases from the closed magnetic field to the open field and achieves the maximum at the center of coronal hole.

In the THM, an additional equation to the governing equations is provided as follows:

$$\frac{\partial E_{st}}{\partial t} + \nabla\cdot(\boldsymbol{u}E_{st}) = -\frac{E_{st} - p(n-4)/2}{\tau_{rel}},$$

where n is the degrees of freedom related to the polytropic index, γ, by $(\gamma-1)^{-1} - (\gamma_0 - 1)^{-1} = (n-4)/2$, E_{st} is the additional internal energy, and τ_{rel} is the relaxation time, which is chosen as the order of the time step.[9] We adopt the same distribution of γ as Cohen *et al.*[2,11] The model adds the source term Q_e, $[E_{st} - p(n-4)/2]/\tau_{rel}$, into basic energy equation.

In the VHM, we add the volumetric heating source Q_e into the energy equation and the momentum source $\boldsymbol{S}_m$ into the momentum equation as carried out

---

*Supported by the National Natural Science Foundation of China (41031066, 40921063, 40874091, 40890162, 40904050, 40874077, and 41074122), and the Specialized Research Fund for State Key Laboratories.

** Email: lpyang@spaceweather.ac.cn

by Feng *et al.*,[5]

$$\begin{aligned} Q_e &= Q_1 \exp(-r) + Q(r-1)\exp(-\frac{r}{L}) \\ &+ \nabla\left(\xi T^{5/2}\frac{\nabla T\cdot\boldsymbol{B}}{B^2}\right)\cdot\boldsymbol{B}, \end{aligned}$$

$$\boldsymbol{S}_m = M(\frac{r}{R_S}-1)\exp(-\frac{r}{L_M})\cdot\boldsymbol{r}/r,$$

where r is the heliocentric distance normalized by the solar radius, Q_1 is the intensity of volumetric heat source, L is the decay length, Q and M are the intensities, which are given to be $Q = Q_0C_a$ and $M = M_0C_a$. The values of Q_1, Q_0, M_0 and L are set to be $1\times10^{-9}\,\mathrm{J\,m^{-3}\,s^{-1}}$, $7.1\times10^{-8}\,\mathrm{J\,m^{-3}\,s^{-1}}$, $5.2\times10^{-14}\,\mathrm{N\,m^{-3}}$ and 0.8, respectively; ξ is chosen to be the same as given by Feng *et al.*[5]

In this study, all three heating methods are initialized with Parker's solar wind solution and the potential field model using the magnetogram for CR 1897, and are solved using the 3D SIP-CESE MHD model. The numerical results are given in the following.

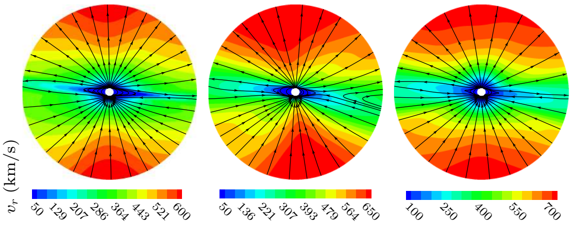

Fig. 1. The calculated steady solar coronal solutions for magnetic field and radial speed v_r in the meridional plane at $\phi = 180°$–$0°$ from 1 to $20R_S$ for the AHM (left), THM (middle), and VHM (right). The color contours represent v_r and streamlines denote the magnetic lines.

Figure 1 is a two-dimensional cut through the 3D steady state model in the meridional plane at $\phi = 180° - 0°$ for 1–20 R_S. We can see that all three heating methods can basically reproduce the bimodal structure with fast wind in the high-latitude region and slow wind near the solar equator (SEQ). From the mid- and high-latitudes (MHL), the magnetic field lines are stretched into the heliosphere by the solar wind and the current sheet forms at the top of streamers. Compared with the coronal results by Linker *et al.*,[14] who used the polytropic relationship in the energy equation, the presence of the heating and acceleration here significantly increases the plasma flow speed from about 400 to 600–700 $\mathrm{km\cdot s^{-1}}$ in the center of the open field region. However, the three heating methods have different effects on the latitudinal extension of the high speed flow. The fast flow ($> 600\,\mathrm{km\cdot s^{-1}}$) at $20R_S$ can extend equatorward roughly to latitudes 50°, 35° and 30° in the AHM, THM and VHM, respectively. The slow flow ($< 600\,\mathrm{km\cdot s^{-1}}$) at $20R_S$ is the widest in the AHM, and the thinnest in the VHM. Additionally, the VHM generates the sharpest cusp structure near the Sun and the AHM produces the furthest cusp structure. In the THM, the magnetic reconnection (MR) occurs near the reversal of magnetic field. The MR was also yielded in the results of Roussev *et al.*[9] and Cohen *et al.*,[2,11] in which the THM was also employed. Thus, the MR is possibly associated with the turbulent heating. The additional heating of the THM in the closed-field region evaporates a small part of coronal streamer,[15,12] increases the electric current around 4–5 R_S, and thus enhances the numerical resistivity, which possibly results in the MR. No excessive heating in the closed field region for the AHM and VHM results in the sharp cusp structures.

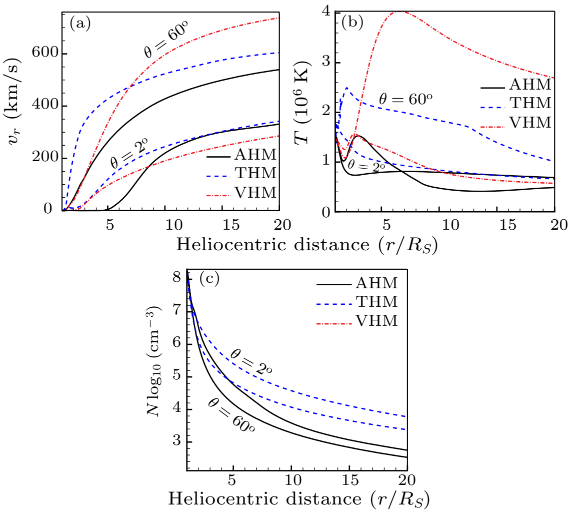

Fig. 2. The radial profiles of the radial speed v_r, the number density N and the temperature T for (a) AHM (solid line), (b) THM (dashed line), (c) VHM (dot-dashed line) at MHL ($\theta = 60°$, $\phi = 0°$) and near SEQ ($\theta = 2°$, $\phi = 0°$).

Figure 2 displays the radial profiles of the flow speed v_r, number density N and temperature T from $1R_S$ to $20R_S$ for the three heating methods. We can see from Fig. 2(a) that the solar wind is accelerated monotonically outward from near the Sun for all the three heating methods. In the VHM and AHM, the plasma flows at MHL are accelerated from about $1.5R_S$ and the major acceleration intervals terminate at $10R_S$. However, in the THM, it lies between $1.2R_S$ and $4R_S$, where the additional energy is mainly deposited. Around SEQ, the near stagnation regions form below $2.5R_S$ in the VHM and $5R_S$ in the AHM, which correspond to the helmet streamers. We also note that the speed in the helmet streamer is about $10\,\mathrm{km\cdot s^{-1}}$ in the THM, which may be due to the heating there. Above the streamer, the plasma bulk speed increases to about $300\,\mathrm{km\cdot s^{-1}}$ at $20R_S$ for all the three heating methods, which agrees with the observations.[16]

Figure 2(b) reveals that the plasma flow at MHL is hotter than that near SEQ for the THM, but the trend only holds true beyond $3R_S$ for the VHM and the reverse relationship exists outside $7R_S$ for the AHM. For the THM, the temperatures both at MHL and near the SEQ quickly rise within $2R_S$ and then drop slowly. For the VHM, the temperature of the plasma flow near SEQ reaches the minimum of 1.3×10^6 K at $1.9R_S$, then the maximum of 1.6×10^6 K at $2.7R_S$, finally drops slowly outward. A similar variation is present in the temperature profile at MHL. However, the temperature profiles for the AHM change in a different way. The temperatures both near SEQ and at the MHL are nearly the same inside $2R_S$. Since then, the former continues falling off to a minimum of 0.75×10^6 K at $2.5R_S$, beyond which the temperature changes little. On the contrary, the latter rises to a maximum of 1.5×10^6 K at $3R_S$ and drops rapidly to the second minimum of 0.5×10^6 K at $13R_S$, and finally increases rather slowly outward.

As shown in Fig. 2(c), the densities for the three heating methods fall off steeply within $10R_S$, and then approach $n\sim r^{-2}$ variation due to the slight increase of the velocities mentioned above. Additionally, the densities near the SEQ are higher than those at MHL for the three heating methods. It should be noted that the densities both at MHL and near SEQ for the THM are much higher than those for the other two heating methods, which probably results from the fact that the major acceleration interval for the THM lies near the Sun, as pointed out by Leer *et al.*[17]

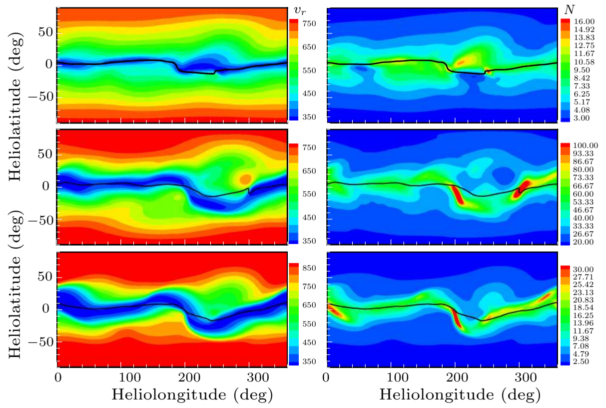

Fig. 3. Contours of radial velocity v_r in units of km·s^{-1} and number density N in units of cm^{-3}) on the surface ($215R_S$) for the AHM (top panels), THM (middle panels), and VHM (bottom panels).

Figure 3 is the distributions of radial velocity v_r and number density N on the surface at $215R_S$. All the three heating methods basically produce the bimodal structure of the fast, tenuous and hot solar wind at MHL and the slow, dense and relatively cool solar wind around the heliospheric current sheet (HCS). We can see that the speeds at MHL are about 750, 750, 850 km·s^{-1} for the AHM, THM, and VHM. Considering the speeds at $20R_S$, we can infer that certain accelerations occur beyond $20R_S$ for all the three methods, among which the fast flow achieves the strongest acceleration for the AHM and the least acceleration for the VHM. However, for all the heating methods, the slow solar winds near SEQ experience very little accelerations out of $20R_S$.

Figure 3 also shows that the areas of both the high-speed (>700 km·s^{-1}) and low-speed (<450 km·s^{-1}) solar winds are the largest for the VHM, and the smallest for the AHM. Additionally, the high-speed solar wind flows in the extended and low-latitude coronal holes for the THM and only in the extended coronal hole for the VHM. However, only the intermediate-speed (450–700 km·s^{-1}) flow appears in the extended or low-latitude coronal holes for the AHM. As a result, there are two corotating interaction regions (CIRs), which result from the high- and intermediate-speed flows overtaking their front low-speed flows, around longitudes $\phi=200°$ and $\phi=300°$ for the THM, one CIR around longitude $\phi=200°$ for the VHM and no CIR for the AHM. The HCS has some twisted structures for the THM and VHM and it is very flat for the AHM.

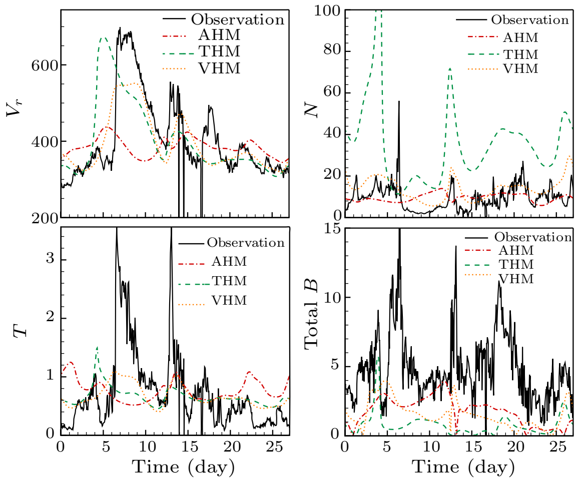

Fig. 4. Comparisons of numerical results with WIND observation (blue line) among bulk flow speed V (unit: km·s^{-1}), proton number density N (unit: cm^{-3}), temperature T (unit: 10^5 K) and total magnetic field magnitude B (unit: nT) for the AHM (red line), THM (green line) and VHM (orange line).

Figure 4 compares the simulation results with the 1-hour averaged observed data of the WIND satellite. It shows that the magnitudes of the solar wind parameters for the three heating methods are located between the observations except that the total magnetic field intensities are sightly smaller than the observations and the number density from the THM is slightly higher. Both the THM and VHM reproduce the overall temporal variations of the solar wind parameters observed by WIND, whereas the AHM does not. Figure 4 demonstrates that the WIND satellite intercepted the intermediate-speed flow from days of 6 to 9 and its associated CIR. Both the THM and VHM capture this intermediate-speed flow and the CIR. It should be noted that the features for the THM are more evident, although they arrived at 1 AU about 2 days earlier. Figures 2–4 infer that the mass fluxes of the high-speed and low-speed flows normalized to 1 AU are about $2.0 \times 10^8\,\mathrm{s^{-1}{\cdot}cm^{-2}}$ and $3.5 \times 10^8\,\mathrm{s^{-1}{\cdot}cm^{-2}}$ for the VHM, $2.0 \times 10^8\,\mathrm{s^{-1}{\cdot}cm^{-2}}$ and $2.5\times 10^8\,\mathrm{s^{-1}{\cdot}cm^{-2}}$ for the AHM and $8.0\times 10^8\,\mathrm{s^{-1}{\cdot}cm^{-2}}$ and $12.0\times 10^8\,\mathrm{s^{-1}{\cdot}cm^{-2}}$ for the THM. The mass fluxes for the VHM and AHM are basically consistent with Ulysses' measurements[18] and the estimation of Wei *et al.*[19] and they are higher for the THM.

In conclusion, all three heating methods can basically reproduce the bimodal pattern of the solar wind observed at 1 AU near the solar minimum. The areas of both the high-speed and low-speed solar winds are the largest for the VHM, and they are the smallest for the AHM. The major acceleration intervals lie between about $1.5R_S$ and $10R_S$ for the AHM and VHM and between 1.2 and $4R_S$ for the THM. At the same time, the results also show that the mass fluxes of the high-speed and low-speed flows normalized to 1 AU are basically compatible with Ulysses' measurements for the VHM and AHM and slightly higher for the THM. Both the THM and VHM roughly reproduce the observed temporal variations of the solar wind parameters and capture the intermediate-speed flows and the features of CIR, whereas the AHM does not. This work also suggests that further studies should be devoted to improving the three heating methods. Here δu_s and Q_e in the AHM, the radius of the source surface in the THM and C_a in the VHM can be tuned to obtain a more realistic solar wind. Additionally, it is necessary to incorporate more available observations and physical-based heating mechanisms[20] into the solar wind simulations.

The simulations were completed on our SIGMA Cluster computing system. We thank the Wilcox Solar Observatory supported by NASA and OmniWeb (http://omniweb.gsfc.nasa.gov/) for providing the observational data. Special thanks go to the anonymous referees for the helpful suggestions.

References

[1] Hassler D M, Rottman G J, Shoub E C and Holzer T E 1990 *Astrophys. J.* **348** 77
[2] Cohen O et al 2007 *Astrophys. J.* **654** L163
[3] Withbroe G L 1988 *Astrophys. J.* **325** 442
[4] Groth C P T et al 2000 *J. Geophys. Res.* **105** 25053
[5] Feng X S et al 2010 *Astrophys. J.* **723** 300
[6] Usmanov A V, Goldstein M L, Besser B P and Fritzer J M 2000 *J. Geophys. Res.* **105**(A6) 12675
[7] Hu Y Q, Habbal S R, Chen Y and Li X 2003 *J. Geophys. Res.* **108**(A10) 1377
[8] Li B, Habbal S R, Li X and Mountford C 2005 *J. Geophys. Res.* **110**(A12) 112
[9] Roussev I I et al 2003 *Astrophys. J.* **595** 57
[10] Hollweg J V 1986 *J. Geophys. Res.* **91**(A4) 4111
[11] Cohen O et al 2008 *J. Geophys. Res.* **113**(A0) 3104
[12] Wang A H, Wu S T, Suess S T and Poletto G 1998 *J. Geophys. Res.* **103**(A2) 1913
[13] Feng X S, Zhou Y F and Wu S T 2007 *Astrophys. J.* **655** 1110
[14] Linker J A et al 1999 *J. Geophys. Res.* **104**(A5) 9809
[15] Suess S T, Wang A H and Wu S T 1996 *J. Geophys. Res.* **101**(A9) 957
[16] Sheeley Jr N R et al 1997 *Astrophys. J.* **484** 472
[17] Leer E and Holzer T E 1980 *J. Geophys. Res.* **85**(A9) 4681
[18] Neugebauer M 1999 *Rev. Geophys.* **37(1)** 107
[19] Wei F, Feng X, Cai H and Zhou Q 2003 *J. Geophys. Res.* **108**(A6) 1238
[20] Cranmer S R 2010 *Astrophys. J.* **710** 676